Compressive Sensing in Massive MIMO Array Testing: A Practical Guide

Stuart F. Gregson, Zhijin Qin, *Senior Member, IEEE*, and Clive G. Parini, *Member, IEEE*

***Abstract*— Compressive sensing (CS) has been deployed in a variety of fields including wideband spectrum sensing, active user detection, and antenna arrays. In massive multiple input multiple output (MIMO) arrays, CS has been applied to reduce the number of measurements required to verify the arrays excitation. To date, the literature has concentrated on the various methods of achieving CS and applying them to both linear and 2-D arrays, and aimed at detecting fully failed elements in an array, offering simple pass/fail testing. All follow the general approach of creating the sparsity needed for CS by subtracting the measured far field or near field of the test array from that of a "gold standard" array measured under exactly identical conditions. This article extended this work to the need for rapid but accurate reconstruction of element excitation in a production testing environment for massive MIMO arrays. The aim is to demonstrate that CS can offer accurate reconstruction of array excitation. Particularly, the work addresses the issues of optimal sampling, measurement noise, accuracy of faulty element detection, effects of beam scanning, and physical alignment of the gold standard array with the test array. We have restricted ourselves to considering production standard arrays with failure rates up to around 5% and conclude with a set of proposed modifications to the basic CS process as applied to array excitations that achieve a near 20 dB improvement in the accuracy of the reconstructed array excitation offering mean square errors (MSEs) near to −40 dB, with a sampling strategy of just 1.4% of the Nyquist rate. This is achieved with the number of measurements to array element size ratio of approximately 0.2.**

***Index Terms*— Antenna measurements, antenna metrology, array antennas, compressive sensing (CS), far-field (FF)-multiprobe anechoic chamber (MPAC), massive multiple input multiple output (MIMO).**

I. Introduction

THE 5th generation new radio (5GNR) promises many new attributes and possibilities; however, perhaps the circa tenfold to 20-fold increase in data capacity is the most significant to the antennas and propagation community as this has mandated the widespread adoption of several new technologies. Chief among these are the use of higher frequency bands and the move to more complex massive multiple input multiple output (MIMO) architectures and beam steering, which are required to manage the associated increased path loss. Although the frequency band below 6 GHz may be used during the initial deployment stage, 5G technologies will mainly operate in the 28 GHz frequency band, or higher, requiring the widespread deployment of more complex, electrically larger, massive MIMO active antenna architectures [1], [2] within the base transceiver station (BTS) system. With the widespread deployment of these complex phased array antennas (typically with several thousand elements), the need to test them comes as part of the production process. Previous techniques developed for high-value, low-volume production, massive arrays used in radar, remote sensing, and satellite communications are time-consuming and inappropriate. Such techniques include using a single low radar cross section (RCS) probe to measure the field close to each array aperture, or the use of near-field/far-field (NF/FF) measurements to verify the FF beam or back project into the aperture to check element excitations [3]. For volume production of massive MIMO arrays, such studies need to be undertaken at the development stage, leading to a reference or "gold" antenna which then needs to be reproduced in volume. Thus, we need to consider methods to reduce the number of measurements needed to determine an array excitation making use of the known excitations of the "gold" antenna.

Compressive sensing (CS) has been deployed in a variety of fields, such as antenna arrays, where a good introduction can be found in [4], active user detection, and wideband spectrum sensing [5]. CS works on the principle that we can reconstruct a big space (P) from just a few samples (S) if we can find a transform that enables the big space to be defined by a few variables in this sparse domain. In antennas, an array of sources can be used to define the whole FF radiation pattern in the forward half hemisphere via the Fourier transform relationship. Thus, the inverse transform from FF to aperture is the "compressed sensing" protocol here. The key to CS is recovering the full measurement from the compressed ones by utilizing the sparsity property [6].

In massive MIMO arrays, CS has been applied to reduce the number of measurements [7]–[9]. Particularly, CS was first applied to the fast spherical near-field (SNF) measurement to reduce the number of measurements by exploiting the sparsity property of spherical mode coefficients (SMCs) [7]. Similarly, CS has been applied to shorten the acquisition time of SNF measurements with a smaller number of measurements and

Manuscript received 16 September 2021; revised 28 January 2022; accepted 16 February 2022. Date of publication 24 June 2022; date of current version 6 October 2022. This work was supported in part by Huawei Research, Munich. *(Corresponding author: Zhijin Qin.)*

Stuart F. Gregson is with Next Phase Measurements, Garden Grove, CA 92841 USA, and also with the School of Electronic Engineering and Computer Science, Queen Mary University of London, London E1 4NZ, U.K. (e-mail: stuart.gregson@qmul.ac.uk).

Zhijin Qin and Clive G. Parini are with the School of Electronic Engineering and Computer Science, Queen Mary University of London, London E1 4NS, U.K. (e-mail: z.qin@qmul.ac.uk; c.g.parini@qmul.ac.uk).

Color versions of one or more figures in this article are available at https://doi.org/10.1109/TAP.2022.3184528.

Digital Object Identifier 10.1109/TAP.2022.3184528

increased measurement speed [8]. Particularly, the pointwise probe correction has been adopted. The developed sampling schemes are applied to nonspherical geometries, which enable the processing of NF measurements obtained in different geometries. Moreover, CS has been applied to reduce the truncation error in cylindrical NF measurements [9]. It has been shown that the reconstruction performance could be improved by exploiting *a priori* information of the antenna under test (AUT) radiation characteristics.

Instead of reducing the number of measurement points required for NF/FF radiation pattern transformation, references [10]–[12] presented the idea of applying CS to array diagnosis from either NF or FF measurements. They assume that the number of failed elements is much less than the total number of elements in the considered array, which is critical to providing the sparsity property required by the successful application of CS. Compared to the other works aiming to reduce the number of measurements, references [10]–[12] reduce the computational complexity in solving the reconstruction problem as the number of defective array elements is usually much smaller than the number of measurement points. This approach requires the availability of the "gold" antenna. Using this approach, Migliore [21] noted the importance of measurement noise in determining the reconstruction accuracy for a given number of faults and samples, and offered design curves to estimate the maximum number of faults, F, that can be accurately detected for a given number of samples, M, with an array size N. For values of F that exceed this limit, the reconstructed excitation mean square error (MSE) rapidly deteriorates. Fuchs and Migliore [13] have further showed that the l_1 reweighted minimization could result in a higher estimation accuracy for the array diagnosis from NF measurements.

In [20], the problem of sample choice is approached from a mathematical deterministic approach based on the criteria to insure that the radiation matrix, A, satisfies the so-called restricted isometry property (RIP). RIP is required to achieve a good reconstruction, and prior to [20], a simple stochastic approach to the choice of sample location was employed. During our preliminary work, we implemented the approach of [20] and found it to work for small linear arrays but not for the large arrays considered here. The highly comprehensive review in [22] of different CS approaches to minimize the number of samples for sparse recovery in spherical antenna NF measurements suggests that RIP is unsuitable for antenna application as it applies to only truly random matrices, and in antenna-based work, the sensing matrix is complex-valued and has no random Gaussian distribution. In addition, they found that the results for the minimum number of measurements using the RIP condition were overly pessimistic.

The Bayesian compressive sensing (BCS) framework [14] was mainly designed to deal with problems with real values. A novel framework has been developed to deal with the real and imaginary components of the array antenna failures [15]. This comprehensive article applies BCS to the "gold" array comparison approach; the work demonstrates that diagnostic errors (DEs) of order -30 dB (0.1%) are achievable with FF measurement to element ratio (M/N) of >0.6 with -40 dB signal-to-noise ratio (SNR). We will see in the following that this MSE can be achieved via conventional convex optimization-based CS with (M/N) of <0.2, thus offering the highly desirable reduced number of FF measurements. BCS is also more complicated to use, thus requiring a number of control parameters to choose before use. However, Salucci *et al.* [15] demonstrate that a much higher failure rates (up to 32%) can be achieved with MSE better than -20 dB, whereas convex optimization-based CS can only achieve about 5%. Our work is aimed at commercial quality arrays in a production environment with a failure rate of $<5\%$, and we have, therefore, chosen the convex optimization route.

To conclude this review of previous work, we return to the comprehensive study of convex optimization-based CS applied to spherical NF sampling [22]. There is much in this work that could be applied to the array fault location problem where limits for minimum number of samples, M, are related to the number of modes (array size, N, in this work) and the sparsity of modes (number of faults, F, in this work) through extensive numerical simulations. It is interesting to note that for -40 dB noise level and M/N of 0.2, the fault detection rate (F/N) is predicted at 5%. We will see that these numbers are what we experience in this study.

In this article, we exploit the fact that the "gold" reference antenna exists and explores the use of CS to undertake a back transform to the array aperture of the difference between the radiation pattern of the AUT and the "gold" antenna using minimal, randomly located, radiated field samples. The aim is to minimize the number of field probes required to measure the antenna in the FF or to minimize the number of NF sample points measured, while accurately reconstructing the array element excitations. The FF multiprobe anechoic chamber (FF-MPAC) is one well-known and widely deployed technique for over-the-air (OTA) testing of 5GNR BTSs, and such a facility either in true FF form or in the more physically compact "reduced FF-MPAC" [16] offers a possible measurement environment for this CS technique. The approach used in this article is summarized in Fig. 1, where the back-projected aperture field indicates just the difference between the aperture field of the AUT and "gold" antenna, and its sparsity enables techniques such as CS to be deployed.

Previous work in this area has mainly used regular or random NF or FF sampling grids and concentrated on pass/fail detection of faulty elements. Here, we consider a practical 2-D array with 192 elements, and we first look at the nonuniform sampling and consider the level of reconstruction accuracy (amplitude and phase via MSE of the complex excitations) that can be achieved for a given number of samples. Then, we propose a number of modifications to the basic CS process as applied to array excitations that achieve a near 20 dB improvement in MSE of the reconstructed array excitation. This work is simulation-based and the aim is to determine key parameters (e.g., SNR, and number and distribution of samples) that can achieve an element excitation MSE of <-30 dB, thus providing a practical implementation guidance to the reader.

The rest of this article is organized as follows. Section II introduces the CS-based defective element detection model.

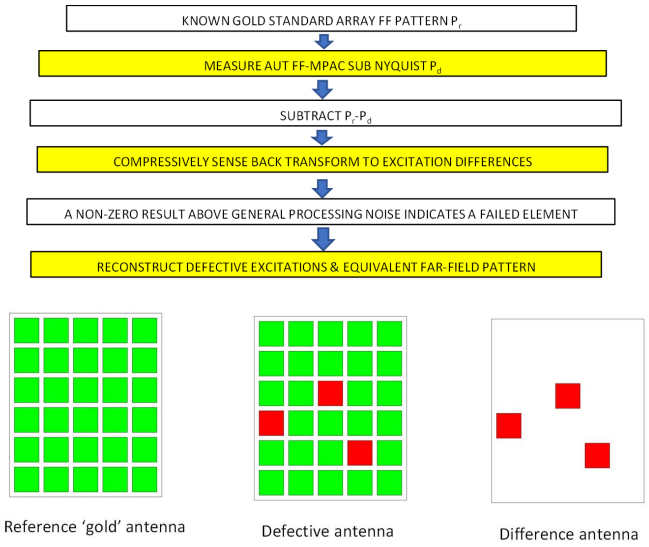

Fig. 1. Flow diagram of defective element detection using CS (top). The "sparse" difference antenna concept (bottom).

Section III presents the application of the developed model to a practical 2-D array, and Section IV considers issues associated with the practical application of the technique. Section V concludes this work.

II. Defective Element Detection Using CS

In the considered system, we assume the availability of the failure-free "gold" antenna array, whose N radiating elements' excitation coefficients are defined as $\boldsymbol{X_r} = \{x_1, \ldots, \boldsymbol{x}_n, \ldots, x_N 1\}^T$, where x_n is the excitation coefficients of the nth radiating element. The corresponding FF pattern vector is denoted as $\boldsymbol{P_r} = \{p_1, \ldots, p_M\}^T$, where p_m is the probe voltage measured at the mth FF sampling point of a total of M sample points. Correspondingly, we denote X_d as the excitations of the (defective) AUT collected at sub-Nyquist sampling rate and P_d as the probe-measured FF pattern collected from the AUT. Then, we consider the following system:

$$\boldsymbol{P} = \boldsymbol{AX} + \boldsymbol{N} \tag{1}$$

where $\boldsymbol{P} = \boldsymbol{P_r} - \boldsymbol{P_d}, \boldsymbol{X} = \boldsymbol{X_r} - \boldsymbol{X_d}, \boldsymbol{N}(0, \sigma^2)$ is the additive white Gaussian noise (AWGN) with zero mean and variance σ^2 and is set by specifying a given SNR for the measurement environment. $\boldsymbol{A} = \boldsymbol{\Psi U}$ and the binary sampling matrix $\boldsymbol{\Psi} \in \boldsymbol{C}^{MxK}$ selects M rows randomly from the discrete Fourier matrix $\boldsymbol{U} \in \boldsymbol{C}^{K\times N}$. Note that the choice influences the recovery performance significantly, which will be discussed in Section III. The element (k, n) of the matrix $\boldsymbol{U}$ is defined as

$$[\boldsymbol{U}]_{k,n} = \frac{1}{\sqrt{N}} \exp\left(-j2\pi \frac{kn}{N}\right) \tag{2}$$

where k is the number of Nyquist sample points. The task of array diagnosis is to detect the faulty elements. We denote the number of faulty elements as F, which is much smaller than the number of radiating elements N. Therefore, $\boldsymbol{X}$ is an F-sparse vector, in which only the faulty elements of the original array contribute to the sparse support. By doing so, we convert the problem into a sparse one. CS can be applied to recover $\boldsymbol{X_d}$ with the knowledge of the excitation coefficients of the "gold" antenna, $\boldsymbol{X_r}$, by solving the following problem:

$$\min_{\boldsymbol{X}} \|\boldsymbol{X}\|_0 \quad s.t.\ \|\boldsymbol{P} - \boldsymbol{AX}\|_2 < \sigma^2 \tag{3}$$

where σ^2 is determined by the noise level affecting the measured samples $\boldsymbol{P_d}$ and P_r. It is noted that the above l_0 problem is nonconvex and difficult to solve. In CS, it has been relaxed to a l_1 problem with guarantee on exact recovery when the RIP is satisfied. Therefore, the optimization problem becomes

$$\min_{\boldsymbol{X}} \|\boldsymbol{X}\|_1 \quad s.t.\ \|\boldsymbol{P} - \boldsymbol{AX}\|_2^2 < \sigma^2. \tag{4}$$

Note that the above l_1 problem is convex, which could be solved by standard convex optimization tools. In this article, we take the cvx toolbox [17] to solve (4). The whole procedure of CS-based defective array detection is summarized in Fig. 1.

It is noted that the reweighted l_1-norm has been proposed in [18] to provide less penalty on the nonzero element in $\boldsymbol{X}$. By introducing the weight to (4), the convex problem is solved in an iterative way. In the lth iteration, the convex problem is solved as

$$\arg\min \sum_{n=1}^{N} \left\| \boldsymbol{w}_n^l \boldsymbol{x}_n^l \right\|_1 \quad s.t.\ \left\| \boldsymbol{P} - \boldsymbol{AX}^l \right\|_2^2 < \sigma^2 \tag{5}$$

where $\boldsymbol{w}_n^l = (1/|\boldsymbol{x}_n^{l-1}| + \eta)$ defines the weight for x_n^l, and η is a small positive constant to ensure the numerical stability of the algorithm. In general, the solution is robust to the choice of η. We note that $\boldsymbol{w}_n^0 = 1$ is taken as the initial value, which makes the reweighted l_1 problem the same as the typical l_1 problem.

The above CS process can be directly applied to a 1-D linear array, where $\boldsymbol{X_d}$ is the recovered excitations. For the case of a 2-D array, we simply wrap this 2-D array of excitations into a 1-D vector while managing the correct phase relationship between the 2-D element and FF radiation. Thus, for a 12 × 16 element array, $\boldsymbol{X_d}$ has dimension 192, and in the following two sections, we will show the application of CS to 2-D array diagnosis.

III. Application to 2-D Arrays

In this section, we take a practical 12 × 16 element massive MIMO array antenna operating at 28 GHz as an example and explore an optimal sampling strategy for the case where the number of defective elements is up to 8, a 4.2% failure rate. The maximum radial extent (MRE) of the array is 67 mm, and from standard sampling theory, the number of plane-wave-spectrum modes required is given by Parini *et al.* [3] as $k_0\text{MRE} + 10 = 49$, where k_0 is the free-space wavenumber, leading to an FF measurement angular spacing of $\delta\theta =$

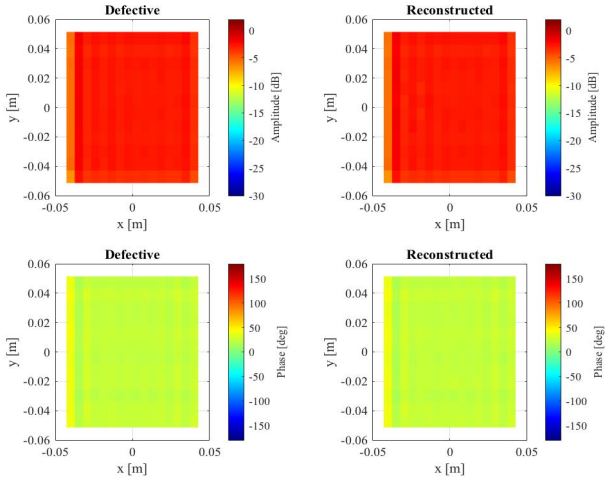

Fig. 2. CST model-based excitations of a 12 × 16 practical massive MIMO array with no defects (left). Reconstructed with −35 dB noise and 36 FF samples giving an element excitation MSE = −40.5 dB (right).

180/49 = 3.6°, requiring 50 × 50 = 2500 FF measurement points at Nyquist sampling. The proposed optimal sampling strategy uses just 36 samples (1.4% of the Nyquist rate).

We have taken a commercial practical array antenna based on patch elements and simulated the radiation characteristics using CST and from this model back projected to the aperture plane to get the elemental excitations. The FF (or NF) radiation pattern of the array obtained from these excitations using a standard Greens function approach provides an FF pattern that includes such effects as mutual coupling. In a fully practical implementation, the FF (or NF) samples of the "gold" and "defective" arrays would be directly measured using, for example, an FF-MPAC facility, and Gregson and Parini [16] describe a physically compact solution to such measurements. Fig. 2 (left) shows the array amplitude and phase excitation derived from the CST model. Fig. 2 (right) shows the CS-reconstructed array excitation when no defects are present but with the measurement undertaken using a noise level of −35 dB relative to the rms level of the FF antenna pattern. We have used this definition of noise as it is more compatible with the wealth of CS work, which is largely based on time signals where root mean square (rms) is the accepted measure. The radiation pattern of our array antenna has an rms level of −25.4 dB below the peak (boresight) level, so in antenna test range terms, the noise level is −60.4 dB relative to the peak. We have taken this level of −60 dB as one that a good quality test range can easily achieve up to 100 GHz (and indeed beyond). The reconstructed pattern of Fig. 2 (right) obtained using just 36 sample points exhibits a MSE of the complex excitation coefficients of −40.5 dB, with a worst excitation error of −28.0 dB amplitude and 2.3° phase. If the level of noise is increased by 10 dB (to 25 dB), the MSE = −31.1 dB and the worst excitation errors increase to −15.9 dB and 3.8°. We will see throughout this article that the measurement noise has a dominant effect on the accuracy of array excitation reconstruction.

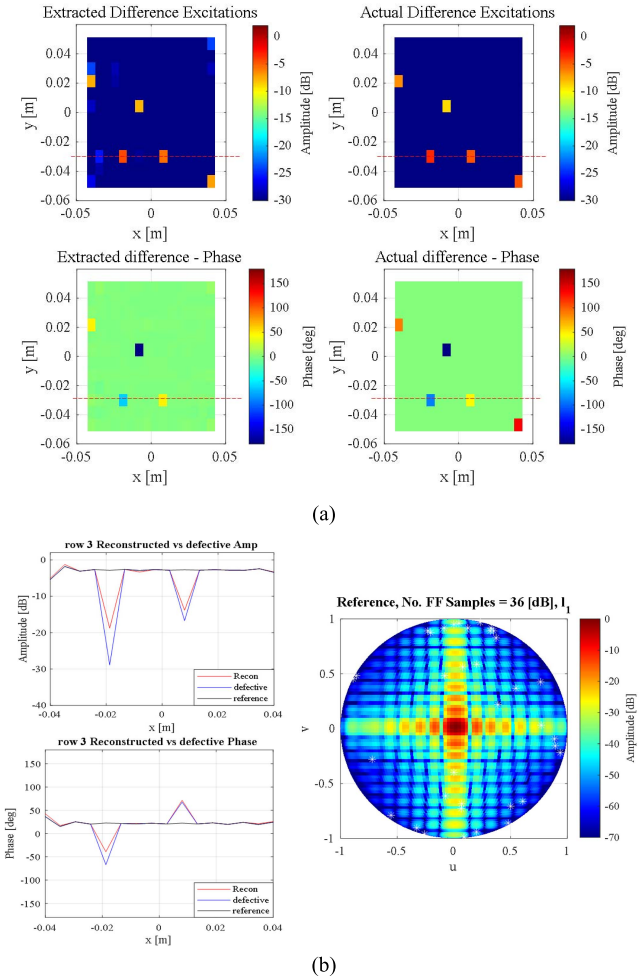

Fig. 3. (a) Extracted difference of array excitations between defective and "gold" array for 36 random samples in azimuth and elevation, five faults, −35 dB noise, and MSE = 29.3 dB (left). Actual difference between defective and "gold" array (right). Dotted line shows the position of excitation detail in (b). (b) Detailed excitation (top amplitude, bottom phase) across dotted line of array shown in (a) for the reference array (black), defective array (blue), and reconstructed array (red) (left). Array FF pattern in u–v space showing sample points taken randomly (white crosses) in azimuth and elevation (right).

The above results are for a near optimal system but first we step back and look at a basic CS system using l_1 and 36 randomly selected FF samples on an azimuth over elevation grid in the forward hemisphere. Fig. 3 shows the results for the array with five faults exhibiting both amplitude errors and phase errors, in the presence of 35 dB noise (as defined above). Fig. 3(a) (left) shows the CS-extracted difference in array excitation between the defective AUT and the "gold standard" (REF) antenna with an MSE = −27.5 dB, and Fig. 3(a) (right) shows the actual (true) difference in the excitation values. This poor value of MSE is attributed in part to the fact that by using random sampling in azimuth and elevation, the sample points cluster around the edges of the direction cosine u–v grid FF pattern of Fig. 3(b) rather than being more uniformly distributed in u–v-direction cosine space.

A. Use of "Smart Sampling"

In this section, we propose a "Smart Sampling" approach where the sampling is random within u–v space and limited to

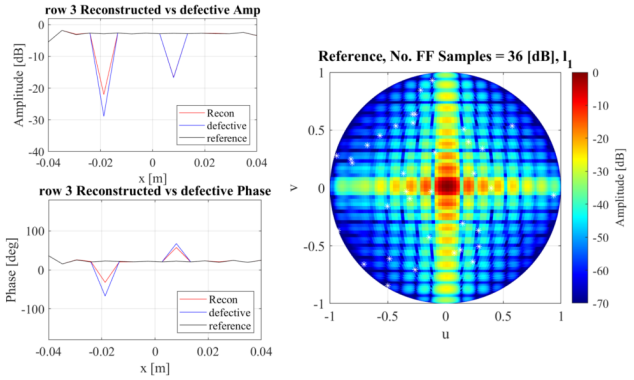

Fig. 4. Result corresponding to Fig. 3(b) for the case of "Smart Sampling" for the 36 sample points.

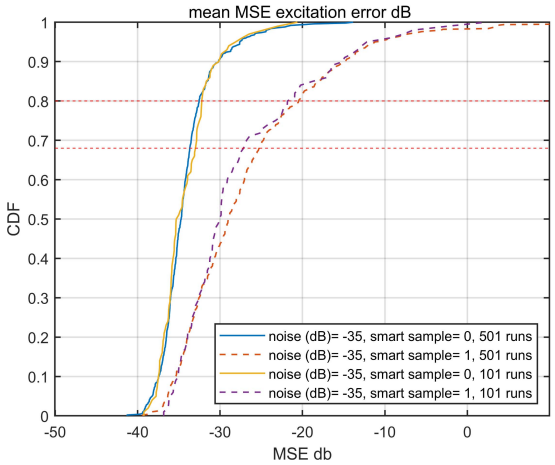

Fig. 5. CDF MSE of reconstructed array excitations for the cases of random Az/El sampling (smart sample = 0) and the smart sampling approach shown in Fig. 3(b) (smart sample = 1), 36 random samples, five random faults, and −35 dB noise.

within the unit circle. Fig. 4 shows the result corresponding to Fig. 3(b) of this approach, showing the sampling points now randomly distributed with a resulting much improved MSE = −35.2 dB.

This result is just a snapshot, and we need to take a statistical view by running the random selection of samples many times and plotting the cumulative distribution function (CDF) of the MSE. This is presented in Fig. 5 where the CDF MSE over 300 runs of 36 random samples with five faults is plotted compared for the cases with and without the "smart sampling" approach in the presence of −35 dB noise. If we take the 80% CDF MSE point as a useful reference point to compare results, then there are 12 excitations using "smart sampling." We have investigated the stability of the CDF MSE statistics for different numbers of runs (50, 100, 300, 500), and for the smart sample = 0 case of Fig. 5, the corresponding 80% CDF MSE values were (−21.9, −21.8, −20.1, −20.4) dB and for the smart sample = 1 case, the corresponding 80% CDF MSE values were (−32.8, −32.2, −32.2, −32.6) dB. The smart sampling = 0 case exhibited a number of cases where the cvx toolbox failed to find a solution, and for different numbers of runs (50, 100, 300, 500), the percentage of failed runs were

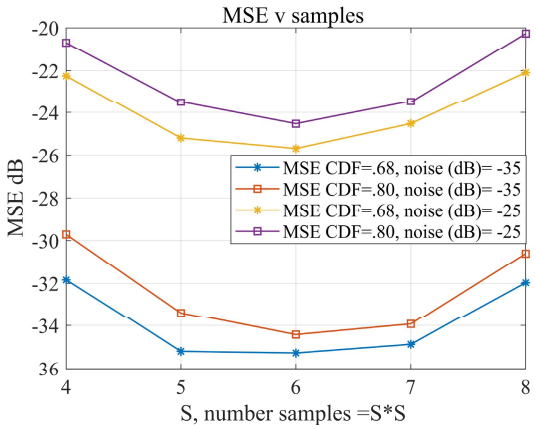

Fig. 6. Search for optimum number of samples for the case of three random faults with noise levels of −35 and −25 dB. Horizontal axis plots the square root of the number of random samples (optimum = 36), and vertical axis MSE at CDF levels of 68% and 80%.

(6, 6, 5, 8) %, respectively. For the smart sample = 1 case, there were no failed solutions in any of the runs, which highlights the fact that smart sampling offers a more robust sampling matrix. Indeed, in the remainder of this work, we have found that the CDF MSE values are fairly steep with CDFs of 0–1 having MSE values spanning around a 10 dB range. For this reason, we have generally taken 100 runs as a statistically valid sample space, and Fig. 5 shows the comparison results for both 100 and 500 runs.

An important question is how many samples, M, need to be taken for a given array size, N, and the number of faulty elements, F, for a given reconstruction MSE. From the presented data in [21] for $N = 101$, we have constructed a very approximate linear equation for maximum number of faults $F \leq 0.55M - N/27$ for the case of reconstructed 80% CDF MSE excitation of −35 and −50 dB of added noise. We have tested this for the cases of $N = 192$ with $M = 25$ and indeed find large deterioration (cliff) in MSE between $F = (6–7)$ as the equation suggests; and with $M = 36$, the cliff occurs between $F = (10–11)$, with equation suggesting (12–13). This sets the smallest M for a given F before the reconstructed element MSE "falls off a cliff"; however, in this work, we seek to find the optimum M giving a good MSE < −30 dB.

In Fig. 6, we search for the optimum number of sample points for the case of smart sampling with three random faults and noise levels of −35 and −25 dB, again with 100 runs per CDF MSE data point. Here, we plot both the 68% (one sigma) and 80% CDF MSE points, as shown in Fig. 5. The horizontal axis plots the square root of the number of samples (S) so the optimum value of 6 corresponds to $M = 36$ random samples.

From this result, we see the dominance of the measurement noise level in determining the MSE, with a 10 dB reduction in noise leading to nearly 10 dB reduction in MSE. The reason for the presence of the optimum at M = 36 is purely down to the presence of measurement noise that results in an increasingly ill-conditioned matrix as the number of samples increases for a given noise level. To illustrate this, we have run Fig. 6 example with noise set at −200 dB for sample values (M) of (36, 100, 400) and find that the 0.68 CDF MSE has

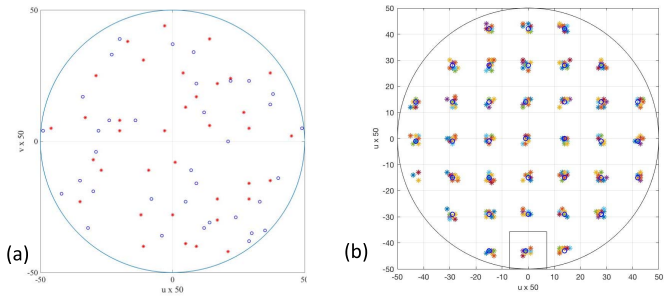

Fig. 7. 36 FF samples taken within the u–v unit circle for: (a) "smart samples" random selection within unit circle (blue circles), pseudorandom samples with rf = 1 (red stars) and (b) ten cases of pseudorandom sampling with rf = 4 (ten different colors) and rf = 64 (blue circles).

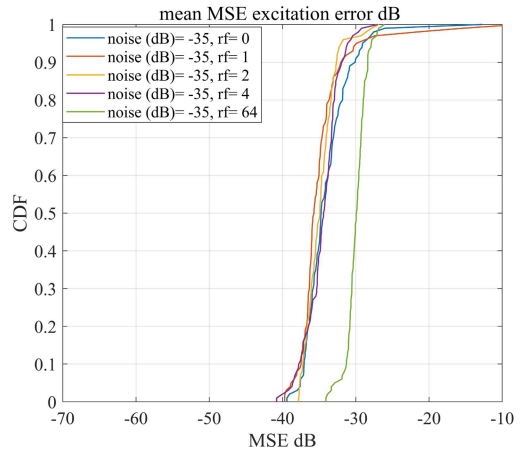

Fig. 8. CDF MSE for different values of pseudorandom sampling parameter rf. Best 80% MSE (−33.6 dB) found with rf = 1. Five random errors and 36 random samples.

continuous reducing values of (−146.7, −152.0, −157.3) dB. A very similar result is seen for the case of five random faults.

We now consider improving the "smart sampling" approach by more evenly distributing the M sampling points across u–v space by dividing the u–v circle into equal-sized square areas and choosing one random point within that area. This we have termed using "pseudorandom sampling," and Fig. 7(a) shows the case for $M = 36$ samples using both "smart sampling" (blue circles) and "pseudorandom sampling" (red stars), with the later showing a more uniform distribution across the u–v unit circle. To achieve the pseudorandom sampling, the circular u–v space is split into a number of equal-sized square regions of size D (with one region shown in Fig. 7(b), bottom-center); the number of these regions is equal to or greater than the desired number of FF samples (M). In this case, 36 samples are required, and the circular u–v region splits symmetrically into 37 square regions, so one of the outer regions is randomly dropped to give 36 samples. Within each square region, one sample point is selected and for the parameter rf = 1, this can be anywhere within the region. For rf = 4, the sample is randomly chosen within a square region of size $D/4$ located at the center of each region. For rf = 64, the square region is so small that only one FF sample, located at the center of the square region, can be selected yielding a

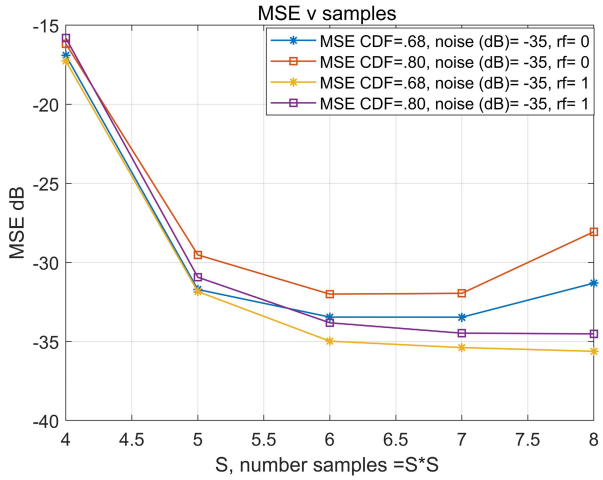

Fig. 9. Smart sampling (rf = 0) and pseudorandom sampling (rf = 1) optimum number of samples for the case of five random faults with a noise level of −35 dB. Horizontal axis plots the square root of the number of random samples (optimum = 36), and vertical axis MSE at CDF levels of 68% and 80%.

fixed periodic sampling grid. Thus, there are 37 clusters of FF points in Fig. 7(b) but only 36 samples in any one sample set (each of the ten sample sets for rf = 4 is shown in a different color to illustrate this).

Fig. 8 shows how the CDF MSE for five random element faults and 36 samples using both the smart sampling method (rf = 0) and the pseudosampling approach described above. Based on this one case, the value of rf = 1 or 2 gives the best result with around 3 dB reduction in the 80% CDF MSE over the rf = 0 case, the "periodic" sample case of rf = 64 being considerably poorer.

Fig. 9 shows a slight improvement in MSE and a flatter curve for pseudorandom sampling (rf = 1) optimum plots compared to the "smart sampling" case of Fig. 6.

B. Use of Reweighted l_1-Norm

In this section, we introduce the reweighted l_1 case [13] (termed rw$l$1) and in Fig. 10 compute the optimum number of pseudorandom samples (rf = 1) for the cases of 1, 3, 5, and 8 random faults with and without the use of rw$l$1. These results show that for this range of random faults (1–8), 36 samples appear to be an optimum choice and that the use of rw$l$1 provides a few dB improvements in reconstructed array excitation MSE in all fault cases.

When the number of samples is smaller, **rw$l$1** provides significantly more improvement in MSE, such as the case with three faults and 16 samples shown in Fig. 10 (top right). Indeed, if we limit our view to a maximum of five faults, then 25 samples provide the best performance. Fig. 11 shows the number of iterations (5) for the rwl1 corresponding to the results of Fig. 10, indicating that for the optimal 36 samples ($S \times S$, $S = 6$), the average number of iterations lies between 3 and 4.

Reconsidering the pseudorandom sampling parameter (rf) with rw$l$1, we find considerable instability in the MSE result as rf is increased. This is illustrated in Fig. 12 where the

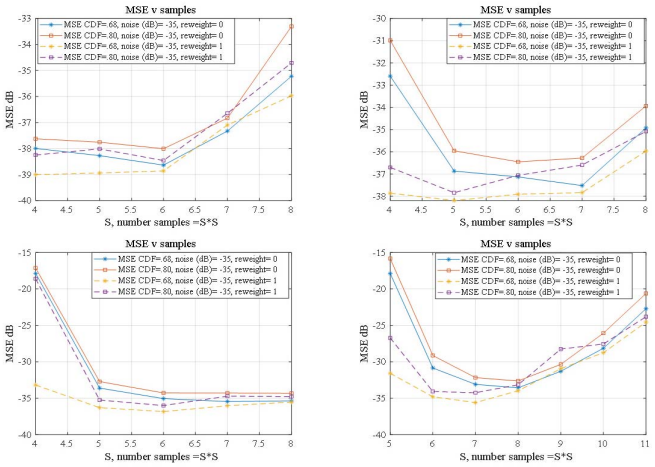

Fig. 10. Optimum number of pseudorandom samples (rf = 1) for the cases of 1 (top left), 3 (top right), 5 (bottom left), and 8 (bottom right) random faults with and without the use of rw*l*1.

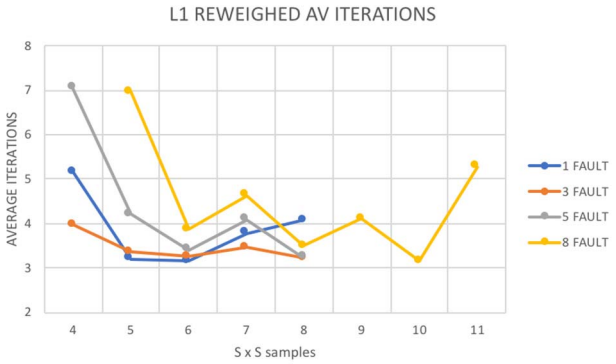

Fig. 11. Number of iterations, in rw*l*1 corresponding to the results of Fig. 10.

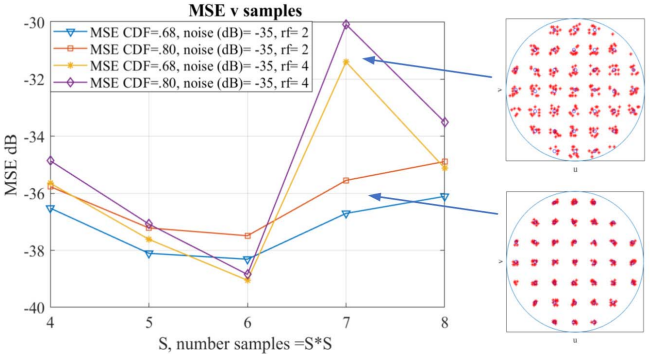

Fig. 12. rw*l*1 with pseudorandom sampling for cases of rf = 2, 4 showing effects of noise and number of random samples for the three random faults case. Insets to figure show the FF sampling grid in u–v space showing in each case of ten sets of samples overlaid for rf = 4 (top) and rf = 2 (bottom).

three random fault case optimum curve is computed for rf = 2, 4. A similar result is seen for rf =1, 64, indicating that moving toward more uniform sampling is not advisable for rw*l*1.

To summarize the results in this section, Table I shows the comparison of the 68% and 80% CDF MSE and corresponding reconstructed rms phase error for the range of faults (1–8) and

TABLE I

DETAILS OF AMPLITUDE AND PHASE ERRORS FOR SMART SAMPLING BASED ON 36 SAMPLES AND THE OPTIMUM (RF = 1) CASE WITH RW*l*1 (LEFT) AND *l*1 (RIGHT)

		rwl1					l1				
faults	noise (dB)	min MSE @68% (dB)	min MSE @80% (dB)	non fifty diag mean err @80% dB	fifty diag mean err - @80 dB	rms phase error, degs	min MSE @68% (dB)	min MSE @80% (dB)	non fifty diag mean err @80% dB	fifty diag mean err - @80 dB	rms phase error, degs
1	-35	-38.9	-38.5	-49.3	-25.9	1.8	-38.6	-38	-49.1	-25.2	2.1
3	-35	-37.9	-37.1	-49.5	-28.4	3.6	-37.1	-36.3	-49.8	-25.2	4.3
5	-35	-36.8	-36	-49.1	-27.3	11.7	-35.1	-34.3	-48.6	-25.2	11.25
8	-35	-34.8	-34.1	-49.1	-26	12.4	-30.9	-29.1	-46	-22.1	12.2
1	-25	-28.5	-28	-39.4	-16.8	5.4	-28.6	-28	-39.4	-15.3	4.9
3	-25	-26.9	-25.9	-38.6	-17.8	11.7	-26	-25.5	-38.4	-14.9	11.6
5	-25	-26	-24.9	-38.7	-17.3	16.6	-25.2	-24.4	-38.2	-15.2	15.9
8	-25	-25	-24	-39.4	-16.7	15.6	-21.7	-20.4	-36.8	-12.4	17.1

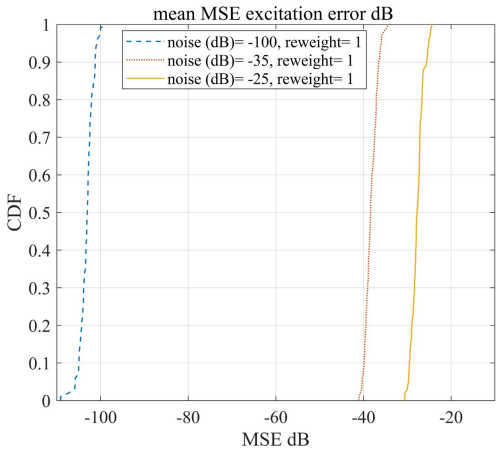

Fig. 13. MSE CDF for 36 fixed samples determined using rf = 1 with five randomly generated defective elements using rw*l*1. Results for 100 test runs for each of three measurement noise levels of (−100, −35, and −25) dB.

measurement noise (−25 and −35 dB) with and without the use of rw*l*1 for the optimal 36 samples. Table I also introduces the concept of DE defined as

$$\mathrm{DE} = 20\mathrm{Log}_{10}(\mathrm{mean}(\mathrm{abs}(\mathrm{recon}(\mathrm{x}) - \mathrm{defect}(\mathrm{x})))) \quad (6)$$

where recon(x) and defect(x) are the complex amplitudes for array element x for the case of the reconstructed and defective array, respectively. In Table I, we have separated DE for the defective elements and the nondefective elements, and these results give insight into the actual levels of accuracy that defective elements can be detected. From the nondefective DE results, it is evident that the level of false alarm is low and with a noise level of −35 dB gives acceptable results for the range of faulty elements up to 8 (4.2% element failure rate).

IV. PRACTICAL IMPLEMENTATION

A practical system with 36 fixed location samples in an FF-MPAC range with sample locations determined from a pseudo randomly generated rf = 1 process has the CDF MSE performance shown in Fig. 13 when rw*l*1 is used with five randomly generated defective elements. We note there is an increasing number of average rw*l*1 iterations as the noise increases from (−100, −35, −25) dB with average iterations of (2, 3.2, 5.9), respectively, indicating the need for the rw*l*1 process to work harder with increasing noise. For the case of −35 dB noise in Fig. 13, running this 100-cycle test result ten times with a different set of 36 sample locations (pseudo

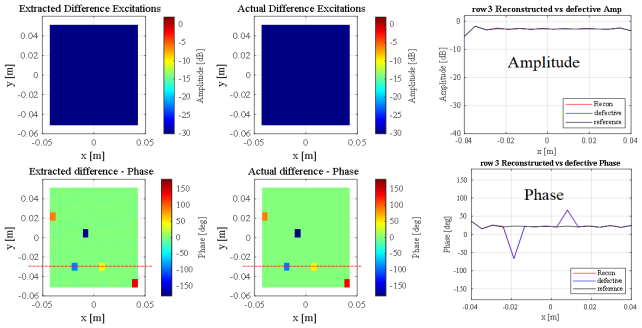

Fig. 14. Optimum 36 fixed samples with five phase-only defective elements and −35 dB measurement noise. MSE = −38.2 dB. Right-hand side plots show amplitude and phase cuts across the array following the red dotted line of row 3. Format of figure follows that of Fig. 3.

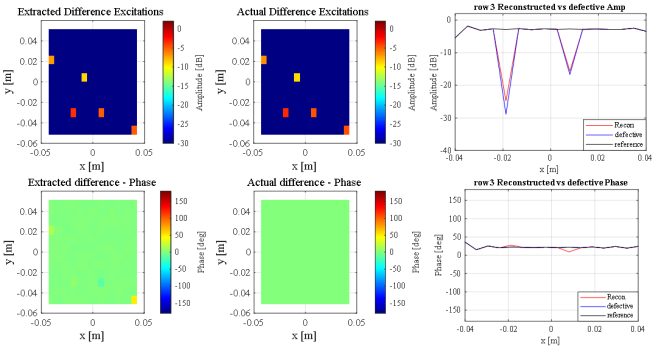

Fig. 15. Optimum 36 fixed samples with five amplitude-only defective elements and −35 dB measurement noise. MSE = −39.9 dB. Format as in Fig. 14 with row 3 amplitude and phase detail on the right.

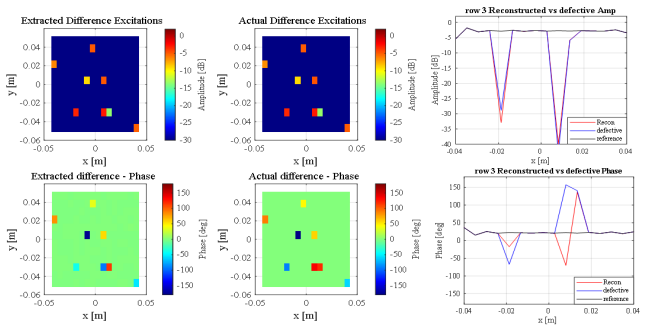

Fig. 16. Optimum 36 fixed samples with eight defective elements, two of which are adjacent element failures in row 3. The −35 dB measurement noise. MSE = −40.2 dB. Format as in Fig. 14 with row 3 amplitude and phase detail on the right.

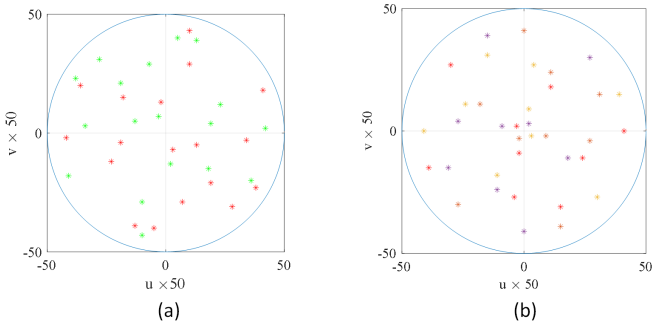

Fig. 17. FF samples in u–v space using phi rotation of AUT to drop the number of physical FF points needed to have 36 samples: (a) red = 18 pseudorandom points and green = same 18 pseudorandom points rotated 180° in phi and (b) nine pseudorandom points taken with phi located at 0°, 90°, 180°, and 270° to form the 36 samples.

randomly generated with rf = 1) yielded a variation in the 80% CDF MSE of ±0.7 dB, so actual choice of the 36 sample points using rf = 1 is not critical.

Fig. 14 shows an example output of the system with five defective elements that are purely phase only, indicating that no amplitude errors are generated by the reconstruction process.

Fig. 15 shows the corresponding results for the case when the five defective elements are amplitude-only defects, indicating a small phase error being associated with a very low level of amplitude (−26 dB) where phase ambiguity will of course be high.

Fig. 16 shows an example output of the system with eight faults including two adjacent elements being defective in row 3, and these adjacent elements have a defective amplitude of 0.01 and 0.7 and defective phase of 135° and 120°, respectively. We note that the phase associated with the element with defective amplitude of 0.01 is poorly reconstructed, again due to phase ambiguity associated with small signal amplitude.

In terms of the cost and complexity of implementation, the fewer the samples taken the better the system. A possible way of reducing the physical number of samples is to take 18 fixed rf = 1 pseudorandom samples and measure the array using two phi angles (0° and 180°) about the array boresight axis. Fig. 17(a) shows this concept for the case where the 18 sample points (red) are measured. The array is then rotated by 180° in phi and the sample remeasured (green points) creating a u–v measurement grid of 36 points overall. Fig. 17(b) shows the same process for nine sample points taken with phi located at 0°, 90°, 180°, and 270°. Fig. 18 shows the comparison of the CDF MSE for the three cases of 36 samples, 18 samples plus one phi rotation of 180°, and nine samples plus three phi rotations of 90°, with the corresponding 80% CDF MSE values showing hardly any difference between the three cases. However, it is important that the core choice of nine samples to create the 36 samples by adding three rotations is well-distributed in u–v space as MSE results can vary wildly. This is shown in the insets of Fig. 18, where a poor choice (left inset) yields a CDF MSE of −18.3 dB compared to the good choice with a CDF MSE of −36.6 dB.

Massive MIMO arrays are beam-scanning antennas, and it is important to verify that CS performance is not impeded by the array antenna beam being scanned.

An alternative use of the AUT phi rotation concept is to provide different sample sets for reconstructing a given defective array. For example, by staying with 36 samples and then rotating the AUT by 180°, we can run the rw*l*1 reconstruction twice and take the average values of each reconstructed array element excitation, thus removing individual outlying MSE values. In Fig. 19, we take the case of 36 fixed

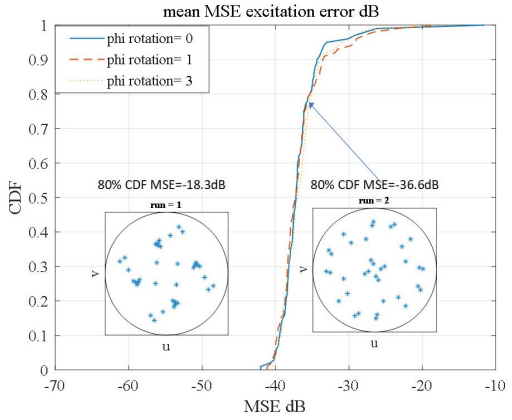

Fig. 18. CDF MSE for the three cases of 36 samples, 18 samples plus one phi rotation, and nine samples plus three phi rotations. Poor choice of the core nine FF samples in u–v space plus three rotations (left inset). The sample set used for main figure result for nine samples plus three rotations (right inset).

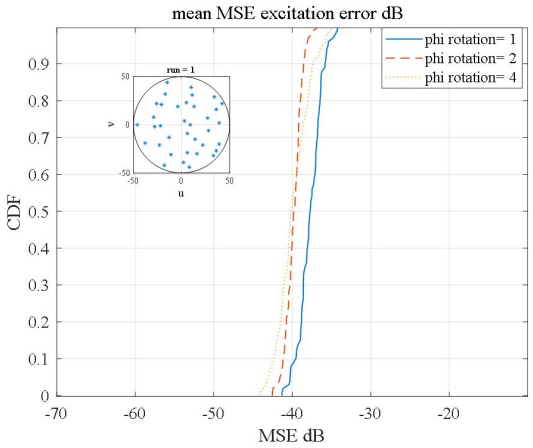

Fig. 19. Thirty-six-sample case without AUT phi rotation and then with both two rotations in phi (180°) and four rotations in phi (90°) with corresponding averaging of each reconstructed array element. The −35 dB noise and rw*l*1.

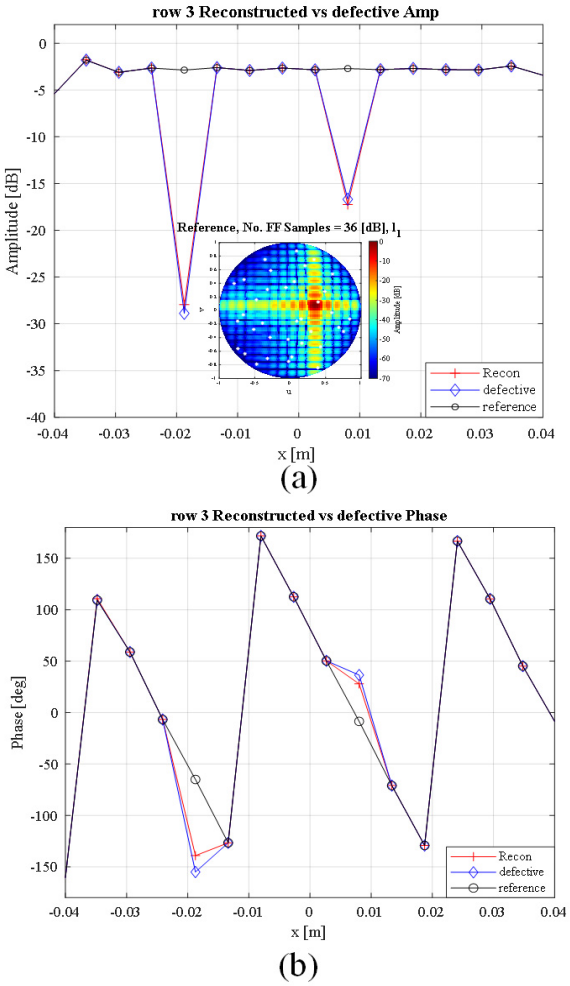

Fig. 20. Cut across row 3 of array excitation showing the reconstructed, defective, and reference array excitations for 36 samples with five defective elements, −35 dB measurement noise, and beam scanned to 10° elevation and 20° azimuth [inset in (a)]. MSE = −40.8 dB: (a) amplitude and (b) phase.

samples and compare the results without rotation and then with two phi positions (0° and 180°) and four phi positions (0°, 90°, 180°, 270°) with corresponding averaging and see several dB improvements in 80% CDF MSE from (−36.5, −39.0, −38.0) dB for (1, 2, 4) rotations, respectively. The four rotation cases (90°) can offer some improvements for low CDF values but of course requiring the fixed probes to be dual-polarized adds complication.

Fig. 20 shows the array with both the amplitude and phase faults of Figs. 14 and 15 but with the beam scanned to 10° elevation and 20° azimuth [FF pattern shown in the inset of Fig. 20(a)]. The reconstructed excitation MSE is unaffected from the nonscanned case, and in Fig. 20(b), we see that the reconstructed phase has the correct taper and the faults are detected (phase associated with the element with failed amplitude of −26 dB is poorly reconstructed, due to the phase ambiguity of small-signal amplitude). Running 100 cases of five random amplitude and phase defects with 36 fixed samples and −35 dB noise gave an 80% CDF MSE of −38.9 dB with the beam scanned and −37.6 dB with no beam scan.

As described in Section I, the developed method relies on subtracting the measured sampled values from the defective array from the measured sampled values of the reference ("gold") array; therefore, mechanical alignment of the array antennas in the antenna measurement facility between "gold" and "defective" AUTs will be an important factor in determining the accuracy of reconstruction process. To investigate this, we consider a small angular mechanical misalignment between the reference and defective arrays when placed in the antenna measurement range, and this is simulated by applying a fractional angular beam scan to the reference (gold) antenna prior to subtraction with the defective antenna pattern. Again, we have taken the case of five random faults and 36 fixed samples with an 80% CDF MSE of −37.6 dB when reference and defective arrays are aligned. With a 0.1° beam scan in both azimuth and elevation applied to the reference antenna, the 80% CDF MSE drops to −30.0 dB and with a 0.05° beam scan, the 80% CDF MSE is −34.2 dB. This gives a measure of the degree of alignment required for the test system. Our

experience of aligning production testing AUTs using dowel pins suggests that values of 0.05° are achievable.

V. Conclusion

Much of the previous CS work has been aimed at detecting fully failed elements in an array, offering simple pass/fail testing. We have extended this work to array element excitation reconstruction through sparse FF (or NF) measurement to the need for rapid but accurate reconstruction of element excitation in a production testing environment. We have demonstrated the advantages of both a smart sampling technique where probe positions are randomly sampled in a direction cosine coordinate system and a pseudorandom sampling technique where samples are randomly selected within a set of evenly distributed cells within the direction cosine coordinate system. The dominant factor of measurement noise has been quantitatively assessed, and we conclude that a viable test system (with reconstructed array excitations MSEs in the high −30 dB range) is possible in an antenna test range with a peak pattern to noise level of 60 dB, a performance achievable in a good quality antenna test range up to at least 100 GHz.

We have concentrated on the application of production testing of massive MIMO arrays with expected array element failure rates of around 4%, and in this case, we have found that a 192-element array with just 36 fixed samples (just 1.4% of Nyquist) enables up to eight faulty elements to be detected with and MSE around −35 dB. We have also demonstrated that by rotating the AUT about its phi axis, the number of sample probes can be reduced down to just nine plus three additional rotations of the AUT to give 36 "random" probe locations. Alternatively, retaining the 36 samples and rotating the AUT in phi can provide an alternative sample set to improve the reconstruction process through averaging. A simple 180° rotation can provide a 2.6 dB improvement in the 80% CDF MSE.

If we consider the basic azimuth/elevation random sample case of Fig. 5 (80% CDF MSE of −20.8 dB) and compare it to using all the aforementioned innovations (pseudorandom sampling, rw$l$1, AUT phi rotation of 180°) with an 80% MSE of −39.0 dB, we see about 18 dB improvement in the reconstructed element excitation MSE value. It should be noted that an MSE of −40 dB represents an excitation amplitude error of 1%, and then, this article has demonstrated that CS can be more than a simple pass/fail test for arrays as well as being able to detect much more subtle errors in element excitations.

Finally, we have assessed the degree of alignment needed between the reference ("gold") antenna and the defective antenna and conclude that 0.05° misalignment in both azimuth and elevation offers minimal degradation to the reconstructed excitation MSE.

This work has been limited to using typical l_1 and reweighted l_1 norms; however, the more sophisticated l_p-norms (with p = 0.1, 0.5) as described in [19] appear to offer further improved results over the l_1 approach. In addition, the application of the spherical NF-based CS work of Hofmann *et al.* [22] to the array element reconstruction problem would be highly valuable in offering a near deterministic choice of minimum number of FF measurements required for a given accuracy of reconstruction.

References

[1] W. Roh, "5G mobile communications for 2020 and beyond-vision and key enabling technologies," in *Proc. IEEE WCNC*, Apr. 2014, pp. 1–49.

[2] Z. Pi and F. Khan, "An introduction to millimeter-wave mobile broadband systems," *IEEE Commun. Mag.*, vol. 49, no. 6, pp. 101–107, Jun. 2011.

[3] C. G. Parini, S. F. Gregson, J. McCormick, and D. Janse van Rensburg, *Theory and Practice of Modern Antenna Range Measurements*, 2nd ed. London, U.K.: IET Press, 2014.

[4] M. D. Migliore, "A simple introduction to compressed sensing/sparse recovery with applications in antenna measurements," *IEEE Antennas Propag. Mag.*, vol. 56, no. 2, pp. 14–26, Apr. 2014.

[5] Z. Qin, J. Fan, Y. Liu, Y. Gao, and G. Y. Li, "Sparse representation for wireless communications: A compressive sensing approach," *IEEE Signal Process. Mag.*, vol. 35, no. 3, pp. 40–58, May 2018.

[6] D. L. Donoho, "Compressed sensing," *IEEE Trans. Inf. Theory*, vol. 52, no. 4, pp. 1289–1306, Apr. 2006.

[7] R. Cornelius, D. Heberling, N. Koep, A. Behboodi, and R. Mathar, "Compressed sensing applied to spherical near-field to far-field transformation," in *Proc. 10th Eur. Conf. Antennas Propag. (EuCAP)*, Davos, Switzerland, Apr. 2016, pp. 1–4.

[8] C. Culotta-Lopez and D. Heberling, "Fast spherical near-field measurements on arbitrary surfaces by application of pointwise probe correction to compressed sampling schemes," in *Proc. Antenna Meas. Techn. Assoc. Symp. (AMTA)*, San Diego, CA, USA, Oct. 2019, pp. 1–6.

[9] M. Salucci, M. D. Migliore, P. Rocca, A. Polo, and A. Massa, "Reliable antenna measurements in a near-field cylindrical setup with a sparsity promoting approach," *IEEE Trans. Antennas Propag.*, vol. 68, no. 5, pp. 4143–4148, May 2020.

[10] M. D. Migliore, "A compressed sensing approach for array diagnosis from a small set of near-field measurements," *IEEE Trans. Antennas Propag.*, vol. 59, no. 6, pp. 2127–2133, Jun. 2011.

[11] B. Fuchs and M. D. Migliore, "Array diagnosis from far field data via ℓ_1 minimizations," in *Proc. 8th Eur. Conf. Antennas Propag. (EuCAP)*, The Hague, The Netherlands, Apr. 2014, pp. 1239–1242.

[12] B. Fuchs, L. Le Coq, and M. D. Migliore, "Fast antenna array diagnosis from a small number of far-field measurements," *IEEE Trans. Antennas Propag.*, vol. 64, no. 6, pp. 2227–2235, Jun. 2016.

[13] B. Fuchs and M. D. Migliore, "Accurate array diagnosis from near-field measurements using ℓ_1 reweighted minimization," in *Proc. IEEE Antennas Propag. Soc. Int. Symp. (APSURSI)*, Orlando, FL, USA, Jul. 2013, pp. 2255–2256.

[14] S. Ji, Y. Xue, and L. Carin, "Bayesian compressive sensing," *IEEE Trans. Signal Process.*, vol. 56, no. 6, pp. 2346–2356, Jun. 2008.

[15] M. Salucci, A. Gelmini, G. Oliveri, and A. Massa, "Planar array diagnosis by means of an advanced Bayesian compressive processing," *IEEE Trans. Antennas Propag.*, vol. 66, no. 11, pp. 5892–5906, Nov. 2018.

[16] S. F. Gregson and C. G. Parini, "Examining and optimising far-field multi-probe anechoic chambers for 5GNR OTA testing of massive MIMO systems," in *Proc. 14th Eur. Conf. Antennas Propag. (EuCAP)*, Mar. 2020, pp. 1–5.

[17] M. Grant and S. P. Boyd. (Sep. 2013). *CVX: MATLAB Software for Disciplined Convex Programming, Version 2.0 Beta*. [Online]. Available: http://cvxr.com/cvx

[18] E. J. Candes, M. B. Wakin, and S. P. Boyd, "Enhancing sparsity by reweighted ℓ_1 minimization," *J. Fourier Anal. Appl.*, vol. 14, pp. 877–905, Oct. 2008.

[19] W. Li, W. Deng, Q. Yang, and M. D. Migliore, "Fast non-convex compressed sensing approach for diagnosis of defective array elements using planar near-field measurements," *IET Microw., Antennas Propag.*, vol. 13, no. 11, pp. 1940–1947, 2019.

[20] W. Li, W. Deng, and M. D. Migliore, "A deterministic far-field sampling strategy for array diagnosis using sparse recovery," *IEEE Antennas Wireless Propag. Lett.*, vol. 17, no. 7, pp. 1261–1265, Jul. 2018.

[21] M. D. Migliore, "Array diagnosis from far-field data using the theory of random partial Fourier matrices," *IEEE Antennas Wireless Propag. Lett.*, vol. 12, pp. 745–748, 2013.

[22] B. Hofmann, O. Neitz, and T. F. Eibert, "On the minimum number of samples for sparse recovery in spherical antenna near-field measurements," *IEEE Trans. Antennas Propag.*, vol. 67, no. 12, pp. 7597–7610, Dec. 2019.

Stuart F. Gregson received the B.Sc. degree in physics and the M.Sc. degree in microwave solid state physics from the University of Portsmouth, Portsmouth, U.K., in 1994 and 1995, respectively, and the Ph.D. degree in near-field antenna measurements and statistical pattern recognition from the Queen Mary University of London (QMUL), London, U.K., in 2003.

He has worked with Airbus Defence and Space, Portsmouth, Leonardo, Edinburgh, U.K., NSI-MI, Los Angeles, CA, USA, and the National Physical Laboratory, Teddington, U.K. He has more than 20 years of experience working in the space, aerospace, and communications sectors and is currently the Director of Operations and Research with Next Phase Measurements, Garden Grove, CA, USA, and also an Honorary Visiting Professor with the School of Electronic Engineering and Computer Science, QMUL. He has developed special experience with near-field antenna measurements, finite-array mutual coupling, computational electromagnetics, installed antenna and radome performance prediction, compact antenna test range design and simulation, electromagnetic scattering, and 5G over-the-air (OTA) measurements, and has authored numerous peer-reviewed research articles on these topics regularly contributing to and organizing industrial courses on these subject areas. At the end of 2007, he was the lead author of the research text *Principles of Planar Near-Field Antenna Measurements*, and in 2014, he has coauthored a second text, *Theory and Practice of Modern Antenna Range Measurements* which is now in its second edition.

Prof. Gregson is a fellow of the Antenna Measurement Techniques Association, the Institution of Engineering and Technology, and the Institute of Physics, and is a Chartered Engineer and a Physicist. In 2018, he was elected to the AMTA Board of Directors where he served first as a Treasurer and subsequently as the Vice-President.

Zhijin Qin (Senior Member, IEEE) received the B.S. degree from the Beijing University of Posts and Telecommunications, Beijing, China, in 2012, and the Ph.D. degree in electronic engineering from the Queen Mary University of London (QMUL), London, U.K. in 2016.

She was a Post-Doctoral Research Associate with Imperial College London, London, from 2016 to 2017, and then a Lecturer with Lancaster University, Lancaster, U.K., from 2017 to 2018. Since 2018, she has been a Lecturer with the School of Electronic Engineering and Computer Science, QMUL. Her research interests include deep learning enabled semantic communications and compressive sensing.

Dr. Qin is serving as an Area Editor of IEEE JOURNAL ON SELECTED AREAS IN COMMUNICATIONS (JSAC) Series on Communications and Networks, and an Associate Editor for IEEE TRANSACTIONS ON COMMUNICATIONS, IEEE COMMUNICATIONS LETTERS, and IEEE TRANSACTIONS ON COGNITIVE COMMUNICATIONS AND NETWORKING. She has served as the Track Chair for IEEE VTC fall 2019 and IEEE GLOBECOM 2020, 2021.

Clive G. Parini (Member, IEEE) joined the Queen Mary University of London, London, U.K., as a Lecturer, in 1977, where he promoted to Reader in 1990 and Professor in 1999 and is currently a Professor of Antenna Engineering and heads the Antenna and Electromagnetics Research Group. He has authored over 400 articles on research topics including array mutual coupling, array beamforming, antenna metrology, microstrip antennas, millimeter-wave compact antenna test ranges, millimeter-wave integrated antennas, metamaterials, and on-body communications. He has coauthored the book entitled *Principles of Planar Near-Field Antenna Measurements*, in 2008, and the book entitled *Theory and Practice of Modern Antenna Range Measurements*, in 2014, which is now in its second edition (2021).

Prof. Parini is a fellow of IET and a Past Member and the Chair of the IET Antennas and Propagation Professional Network Executive Team. He is a Past Member of the Editorial Board and a Past Honorary Editor of the *IET Microwaves, Antennas & Propagation*. In 2009, he was elected as a fellow of the Royal Academy of Engineering. In 1990, he was one of the three coworkers to receive the IEE Measurements Prize for work on near-field reflector metrology. In 2002, along with several coworkers, he was awarded the BAE SYSTEMS Chairman's Bronze Award for Innovation for work on microwave near-field metrology.